



# Laser-Directed Energy Deposition of Dissimilar Maraging Steels with a Defect-Free Interface: Design for Improved Surface Hardness and Fracture Toughness

Faraz Deirmina<sup>1,5</sup> · Sasan Amirabdollahian<sup>2</sup> · Luke Harris<sup>3</sup> · Eleonora Bettini<sup>1</sup> · Raveendra Siriki<sup>4</sup> · Massimo Pellizzari<sup>2</sup> · Paolo Bosetti<sup>2</sup> · Alberto Molinari<sup>2</sup>

Received: 8 December 2022 / Accepted: 20 February 2023 / Published online: 9 May 2023  
© The Author(s) 2023

## Abstract

Maraging steels are a class of low-carbon ultra-high-strength martensitic steels. Due to their excellent weldability, these steels have been widely applied for laser-based additive manufacturing (AM). MAR-60HRC is a newly developed maraging grade for AM with a nominal chemical composition of 13.0Ni-15.0Co-10.0Mo-0.2Ti, Fe bal. (wt%), capable of achieving hardness levels of ~ 740 HV. Alternatively, 18Ni300 is a commercialized maraging steel with an excellent combination of strength and toughness at the peak aged hardness (i.e., ~ 590 HV). This work aims to investigate the properties and microstructure of MAR-60HRC fabricated by Laser Directed Energy Deposition (L-DED). Further, the manufacturability of bimetallic parts comprising a tough 18Ni300 core and a hard MAR-60HRC on the surface was evaluated. After proper aging, the multi-layered material showed a surface hardness of ~ 720 HV1 and apparent fracture toughness of 71 MPa m<sup>1/2</sup>, higher than that of MAR-60HRC (i.e., 60 MPa m<sup>1/2</sup>), and lower than 18Ni300 (i.e., 90 MPa m<sup>1/2</sup>). The excellent combination of surface hardness and fracture toughness was discussed, considering the crack arrest at the interface and the flawless interface between the two steels.

**Keywords** Additive manufacturing · Maraging steels · Bimetal · Crack arrest · Hardness · Fracture toughness

---

Faraz Deirmina and Sasan Amirabdollahian have equally contributed to this work.

---

✉ Alberto Molinari  
alberto.molinari@unitn.it

Sasan Amirabdollahian  
s.amirabdollahian@gmail.com

Eleonora Bettini  
Eleonora.Bettini@sandvik.com

<sup>1</sup> Powder R&D, Sandvik Additive Manufacturing, Sandvik Machining Solutions AB, Mossvägen 10, 811 82 Sandviken, Sweden

<sup>2</sup> Department of Industrial Engineering, University of Trento, Via Sommarive 9, 38123 Trento, Italy

<sup>3</sup> Powder Group, Sandvik Additive Manufacturing, Milland Road, Neath, UK

<sup>4</sup> Alleima (Sandvik Materials Technology), Sandviken, Sweden

<sup>5</sup> Siemens Energy AB, Norrköping, Sweden

## 1 Introduction

Additive manufacturing (AM) technologies are receiving ever-increasing attention in recent years due to their unique characteristics in the production of complex geometries in a short time and sustainable way for a variety of materials [1]–3. Laser-directed energy deposition (L-DED) is one of the most practiced AM technologies for manufacturing metallic components due to its distinctive capacities in developing functionally graded materials and cladding. Moreover, compared to traditional repair technologies, such as arc welding, TIG welding, and plasma welding, L-DED shows several advantages such as relatively lower heat input, less distortion, lower dilution rate, and relatively higher geometrical accuracy that makes it a suitable option for repair and restoration as well [4]. L-DED has found its application mainly in the fields of wear protection, repair, and maintenance of high-value parts, such as tools, molds, and aerospace components made from Fe-, Ti-, and Ni-based alloys [5].

Maraging steels are a class of high-performance, low-carbon martensitic steels that combine ultra-high strength ( $UTS > \approx 1800$  MPa) and high toughness [6]. The relatively soft and tough Fe–Ni martensite can be age-hardened by the precipitation of nano-sized intermetallic particles containing substitutional alloying elements (e.g., Mo, Ti, Al) through a simple heat treatment. The addition of Co in this alloy system raises the martensite start ( $M_s$ ) temperature, enabling the addition of more substitutional alloying elements (e.g., Mo) without the risk of stabilizing retained austenite [7]. Moreover, Co increases the supersaturation of Mo in the matrix, providing an increased amount of this element taking part in precipitation. The combination of Co with a specific weight percentage of Mo, as in the Mo-containing quaternary alloys (Fe–18Ni–Co–Mo), increases the strength by up to 500 MPa [7, 8]. Ti is the other alloying element contributing to age hardening at low weight percentages (i.e., 0.2 to  $\sim 2.0$  wt%) [9]. Depending on the alloying elements, the main intermetallic strengthening compounds in these systems are orthorhombic  $Ni_3(Mo)$ , hexagonal  $Ni_3(Ti, Al)$ , rhombohedral  $Fe_7Mo_6$   $\mu$  phase, hexagonal  $Fe_2Mo$  Laves phase, hexagonal  $\omega$  phase,  $Ti_6Si_7Ni_{16}$  G phase, and  $A_3B$  hexagonal "S phase" [9]–13. In recent years, several Fe–18Ni–Co–Mo alloys have been developed on an industrial and research scale [14]–15, and Ni–Co–Mo compositions with lower Ni content, as well as Co-free classes, have been assessed [16]–21. Due to the high Ni content and the absence of C (less than 0.03wt%), hardenability is not an issue in these alloys, and hence cooling rate after solution annealing treatments is not critical [8]. In the solution annealed condition, the alloys, depending on the type and content of alloying elements, show hardness of the order of 30 HRC. Parts can be thus readily machined. Additional hardening can be achieved by aging at the recommended temperatures and times [22]. Dimensional changes after aging treatments are generally negligible, thus enabling finishing operations to be carried out on the parts before age hardening. They also show good polishability [8, 14]. More importantly, their excellent toughness at high strength levels makes this steel class an ideal candidate for use in applications requiring high strength-to-weight ratios [14, 23]. Maraging steels are therefore considered viable materials for tooling applications such as injection molds, extrusion tools, die-casting dies, core pins, and cores, as well as for structural applications [14]. The fracture toughness versus hardness for some of the maraging steel available in the literature is presented in Fig. 1. As expected, by increasing the hardness, a drop in fracture toughness is evident.

Due to their excellent weldability even without preheating and negligible dimensional changes after age hardening, maraging steels have been exploited commercially in near net-shape AM processes such as laser powder bed fusion (L-PBF) and directed energy deposition (DED) [28]. On an

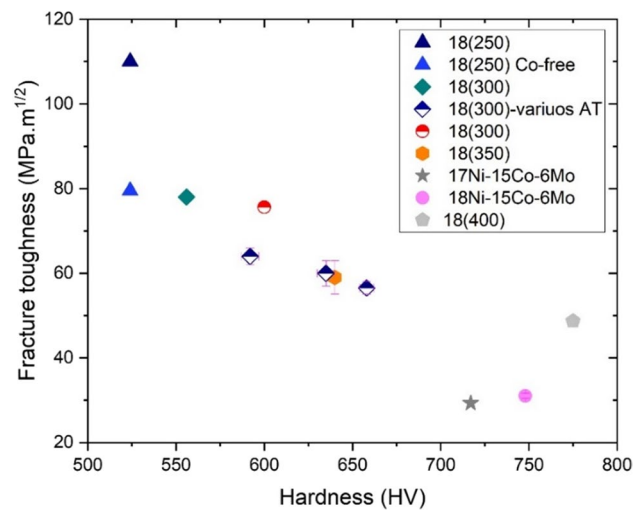


**Fig. 1** Fracture toughness vs. Hardness for different maraging steels. Half-filled symbols belong to AM samples [19, 24].–[27]

industrial scale, parts in 18Ni300 (18.0Ni–9.0Co–4.5Mo–0.7Ti–0.1Al, Fe bal. (wt%)) with complex geometries and enhanced mechanical properties have already been commercialized [29]. This steel shows a peak hardness of  $\sim 600$  HV, and tensile strength of  $\sim 2000$  MPa, with good ductility and toughness. However, in certain applications, a further increase in hardness aimed at increasing the wear resistance of 18Ni300 has been considered a crucial requirement. This led to the development of Osprey® MAR-60HRC (hereafter, MAR-60HRC), showing a maximum achievable hardness of  $\sim 61$  HRC and ultimate tensile strength of  $\sim 2600$  MPa [30]. The higher Co and Mo content in this alloy gives rise to higher vol% and enhanced  $Ni_3Mo$  and  $\mu$  phase precipitation kinetics leading to higher hardness after aging.

Other than alloy modification, the hardness can be increased by the addition of hard ceramic particles to fabricate AM 18Ni300 metal matrix composites. However, it is reported that substantial additions of reinforcing particles result in collision and agglomeration of un-melted/un-dissolved ceramic particles with much higher melting points than that of the matrix to the sides of the melt pools [31, 32]. The stabilization of retained austenite using carbon-containing ceramic particles such as TiC and WC is also documented, and interfacial reactions between the matrix and the reinforcement leading to the embrittlement of the interface are witnessed in some research works [31, 33, 34]. More importantly, mixing the ceramic particles with steel powders introduces an additional step to the process chain with the risk of powder contamination. In other studies, plasma nitriding has been applied to increase the surface hardness of 18Ni300 [35]–37. The process is assessed to increase the surface hardness of AM-18Ni300 both in the direct aging and after solution annealing aging. The surface hardness is reported to reach up to  $1000$  HV<sub>0.01</sub>, and

it declined to  $\sim 700$  HV<sub>0.01</sub> within 30  $\mu\text{m}$  from the surface and gradually dropped to the value of the base material at a depth of  $\sim 100$   $\mu\text{m}$ . The presence of some connected pores and cracks in the compound layer of the nitrated zone and the formation of discrete TiN particles are reported for the nitriding of AM-18Ni300 [37]. An alternative approach for realizing parts with different properties on the surface and at the core is producing bimetal. To date, few studies have investigated the fabrication of bimetal of maraging steels [38, 39], and these studies are limited to selective laser melting (SLM) of maraging steels on a tool steel baseplate. The different heat treatment responses of these materials might be a limiting factor in some applications.

Nearly all engineering structural materials must meet both strength and toughness requirements, however, most materials cannot exhibit both of these qualities simultaneously [40]. A solution to promote toughness in hard materials is to exploit extrinsic toughening mechanisms, e.g. crack deflection, zone shielding (transformation toughening, crack tip dislocation shielding, residual stress fields), or contact shielding (bridging, wedging, sliding) [41]. The peculiar micro/mesostructure of additively manufactured parts can be exploited in this regard. Suryawanshi et. al [42] demonstrated that heterogeneous microstructure in Al-12Si parts produced by SLM resulted in higher fracture toughness due to crack deflection (tortuous crack path). Huang et.al [43] exhibited that in in-situ alloyed Ti41Nb, alternating Nb-poor regions (NPRs) at melt-pool boundaries resulted in a layered composite mesostructure that favored extrinsic toughening through crack deflection. In their pioneer work, Kürnsteiner et. al. utilized the intrinsic heat treatment (IHT) by tuning the thermal history through the application of proper interlayer dwell times, to obtain an alternating mesostructure of hard and soft layers for a Fe19Ni5Ti steel produced by L-DED and demonstrated a marginal improvement of impact toughness for this steel at cryogenic and room temperatures at a higher tensile strength compared with the uniform microstructure, and a notable improvement at 200 °C [44].

In the current work, we studied the heat treatment and microstructure of MAR-60HRC fabricated by L-DED; further, we report the surface engineering of an L-DED 18Ni300 substrate by deposition of MAR-60HRC using L-DED. The fully compatible chemical compositions of these two alloys (i.e., both comprise Ni, Co, Mo, and Ti, as alloying elements) should give the advantage of forming a clean interface with strong metallurgical bonding. The thickness of the harder MAR-60HRC can be freely increased to increase the load-bearing capability of the component. The proposed design

should benefit both from the high hardness of MAR-60HRC on the surface and the excellent toughness of the core 18Ni300, leading to a damage-tolerant material with an extremely high surface hardness which can be specifically beneficial for tooling applications by improving wear resistance.

## 2 Materials and Methods

Gas atomized OSPREY<sup>®</sup> MAR-60HRC, and 18Ni300 maraging steel powders with a particle size distribution ( $-105$   $\mu\text{m} + 50$   $\mu\text{m}$ ) were used for depositions. The nominal composition of the powders is presented in Table 1.

Deposition of samples was carried out using a LASERTEC 65 3D hybrid machine (DMG MORI AG) with a 2500W diode laser ( $\lambda = 1020$  nm) and a Coax 14 nozzle. The laser has a top-hat beam profile with a spot diameter of 3 mm at a focal length of 13 mm. After undertaking a series of process optimization tests to obtain the optimum processing parameters, samples were deposited with the processing parameters listed in Table 2. A meander scanning strategy with 90 ° rotation between successive layers was applied. Argon was used as the carrier and shielding gas with a flow rate of 5 and 5.5 l/min, respectively. Samples with a relative density of 99.5%, measured using the Archimedes method, were obtained.

Aging heat treatments were performed using an L75 Platinum LINSEIS dilatometer in an Argon atmosphere. Samples were age hardened at different temperatures and times to obtain the aging curves. All aging treatments were carried out by direct aging of the as-built specimens.

Cuboid samples (45 mm  $\times$  10 mm  $\times$  35 mm) were deposited using the parameters described above (Table 2). Three single-edge notched bend (SENB) specimens (6 mm  $\times$  3 mm  $\times$  30 mm) were cut out of cuboids for each material using wire electro-discharge machining (EDM) (Fig. 2). Finally, a notch ( $a/w = 0.5$ ,  $\rho = 90$   $\mu\text{m}$ ) was introduced in the samples by EDM. Following the results obtained from aging curves, samples were heat-treated

**Table 2** L-DED processing parameters

Parameter	Laser power (W)	Scanning speed (mm/min)	Powder feed rate (g/min)
MAR-60HRC	1700	1300	12
18Ni300	1800	1200	12

**Table 1** The nominal composition of the MAR-60HRC and 18Ni300 powders in wt%

Element	Ni	Co	Mo	Ti	Al	C	Fe
MAR-60HRC	13.0	15.0	10.0	<0.2	<0.1	<0.03	Bal.
18Ni300	18.0	9.5	4.7	0.7	<0.1	<0.03	Bal.

**Fig. 2** Schematic of the samples prepared for fracture toughness tests



directly from the as-built condition at 480 °C for 6 h prior to experiments. Plane strain fracture toughness testing was performed using 3-point bending tests under stroke control at a rate of 0.5 mm·min<sup>-1</sup> using a 1343 Instron machine equipped with a 5 kN load cell. In the plane strain testing conditions, the stress concentration factor decreases with increasing the root radii [45], and higher applied stress is thus needed to reach the "critical stress intensity." This leads to slightly higher apparent fracture toughness ( $K_{app}$ ) compared with that of the plane strain fracture toughness ( $K_{IC}$ ) obtained with fatigue pre-cracked specimen (i.e.,  $\rho \rightarrow 0$ ). It should be noted that fracture toughness data obtained in this study should not be used directly in the design of structural elements, and are intended only for comparison between different specimens within this study, which have all undergone identical EDM processes. Despite the large notch radius, the  $K_{app}$  values do not appear to vary significantly below a critical radius ( $\rho = 100 \mu\text{m}$ ) [45], therefore the  $K_{app}$  values are still useful for comparative analysis.

In bimetallic samples, the notch was realized in the harder material (i.e., MAR-60HRC), as shown in Fig. 2. A distance ( $l$ ) of  $\sim 800 \mu\text{m}$  between the interface and notch root was considered. In this condition, the plastic zone radius ( $r_y$ ) [46] ahead of the notch, conservatively calculated through Eq. 1 considering the critical value of stress intensity ( $K_{app}$ ) for MAR-60HRC (i.e.,  $60 \text{ MPa m}^{1/2}$  obtained using a crack tip radius of  $90 \mu\text{m}$ ), and the yield strength of the softer material ( $\sigma_y$  18Ni300  $\sim 1950 \text{ MPa}$  [47]), is  $500 \mu\text{m}$ , thus smaller than  $l$ . It is important to remark that the  $K_{app}$  numbers in this work cannot be used as a measure for the  $K_{IC}$  of the material. However, by using the apparent fracture toughness obtained with the current test method, which is larger than that of standard  $K_{IC}$  (i.e.,  $30 \text{ MPa m}^{1/2}$ ) reported for the wrought counterparts with almost similar chemical composition, and aged hardness [19, 48], the calculated plastic zone radius will be overestimated by around four times. This overestimation plausibly satisfies the condition after which, the plastic zone near the notch tip ( $\sim 500 \mu\text{m}$ ) is still within the MAR60HRC region, far enough from the interface (i.e.,  $800 \mu\text{m}$ ) [46]. As a result of reducing the complexity in the plastic zone by excluding the effect of 18Ni300, interpretation of the fracture toughness of the bimetal, in particular, the direct influence of the interface and its interaction with the

unstable crack propagation from MAR-60HRC towards 18Ni300 can be analyzed.

$$r_y = \frac{1}{6\pi} \left( \frac{K}{\sigma_y} \right)^2 \quad (1)$$

Metallographic cross-sections were prepared by grinding up to 1200 grit, subsequent polishing with  $3 \mu\text{m}$  and  $1 \mu\text{m}$  diamond pastes, followed by a final oxide polishing. Microstructural characterizations were done on metallographic cross-sections chemically etched by Vilella's reagent, using both light optical microscope (LOM) (Zeiss Axiophot) and scanning electron microscopy (SEM) (Jeol JSM-IT300LV). SEM was also employed to characterize the fracture surfaces. Electron backscattered diffraction (EBSD) combined with electron dispersive x-ray spectroscopy (EDS) elemental mapping was carried out using a Symmetry EBSD detector on a Field Emission Gun Scanning Electron Microscopy (FE-SEM, Zeiss Sigma, Germany) on oxide-polished cross-sections to investigate the phase constitutions and semi-quantitative elemental analysis, respectively. XRD analysis on age-hardened samples was carried out using an Italstructures (IPD3000/CPS120) instrument equipped with a Co  $K\alpha$  source of 2000 W ( $\lambda = 0.17889 \text{ nm}$ ). The angular step size and integration time were  $0.03^\circ$  and 4 s, respectively. XRD spectra were then analyzed using MAUD software [49] to quantify the phases. Hardness (HV1) measurements were performed according to ASTM E92-17.

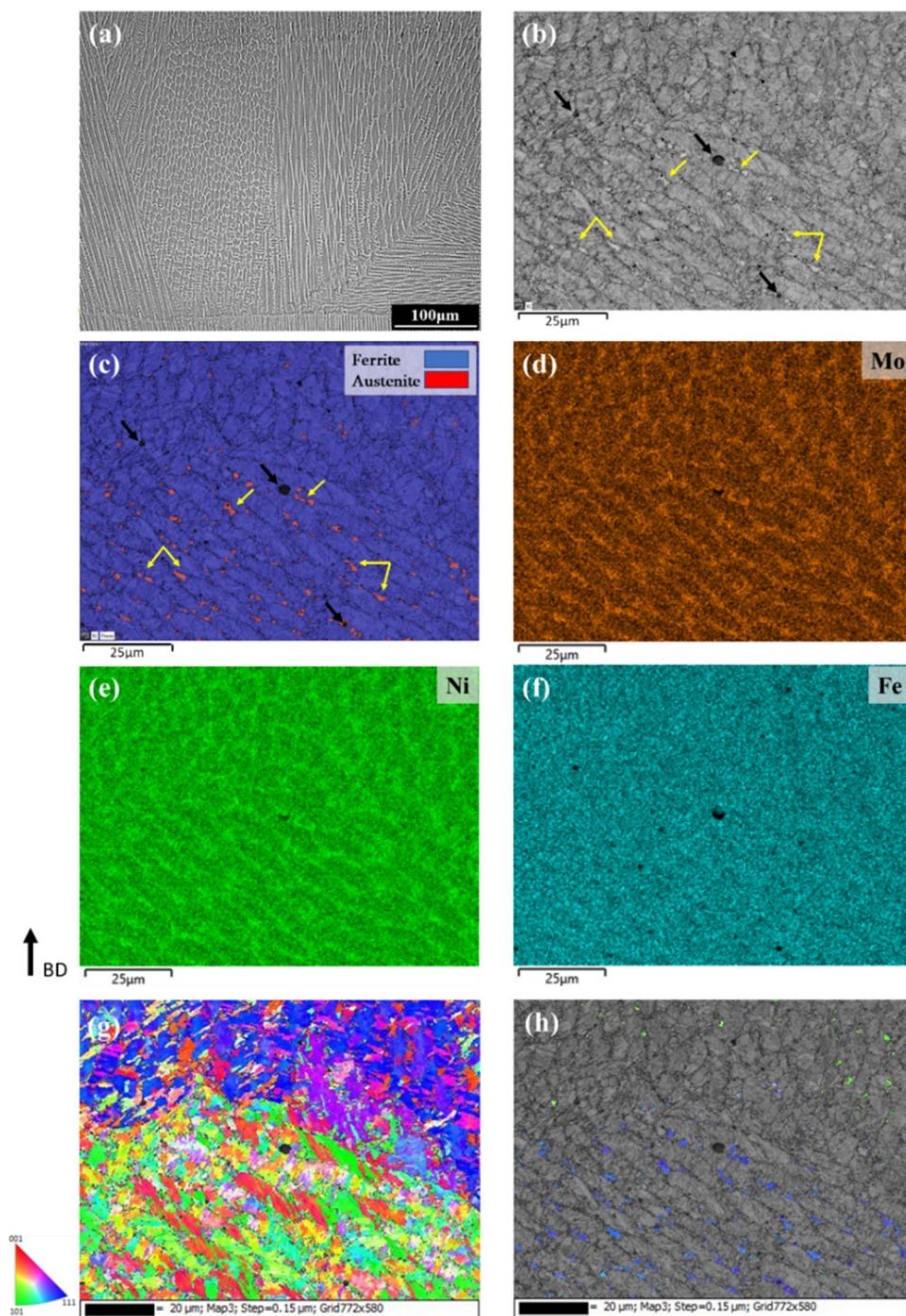
## 3 Results and Discussion

### 3.1 Microstructure and Hardness of L-DED MAR-60HRC

The microstructure of the deposited as-built samples comprises fine cellular/dendritic features (Fig. 3a). EBSD band contrast and phase maps revealed the presence of retained austenite (RA) located in the intercellular regions (yellow arrows in Fig. 3b and c). Corresponding EDS maps evidenced a higher concentration of Mo and Ni and a lower Fe content in the intercellular areas (Fig. 3d-f). The driving force for dendrite/cell nucleation and growth is provided by thermal undercooling. The microsegregation of alloying elements to the cell/dendrite boundaries occurs due to solute



**Fig. 3** **a** LOM micrograph showing the overall microstructure of the L-DED MAR-60HRC (Vilella's reagent), **b** EBSD band contrast image, **c** Corresponding phase map overlaid by band contrast image, and corresponding EDS elemental map for **d** Mo, **e** Ni, **f** Fe, **g** IPF maps of martensite, and **h** IPF maps RA with respect to build-direction



partitioning in liquid and limited solid-state diffusion during fast solidification, characteristic of laser-based AM processes such as L-DED [50]. The micro-segregation of alloying elements at cell boundaries leads to the chemical stabilization of RA in those areas [1]. Inverse pole figure (IPF) maps of martensite (formed inside the prior austenite grains) and retained austenite along the build direction are presented in Fig. 3g and h. It can be clearly noted that the crystal orientation of the RA is related to the prior austenite grain

orientation. The RA in the bottom grain is oriented closer to  $\langle 111 \rangle$  while in the top grain is along  $\langle 110 \rangle$  direction.

The fine and mostly round particles (black arrows in Fig. 3b and c), having a size from a hundred nm to a few micrometers, are rich in Ti (26 at%), Al (11 at%), and O (61 at%) are plausibly Ti- Al-rich oxides, close to  $(\text{Ti}, \text{Al})_2\text{O}_3$  stoichiometry. Due to the high affinity of Ti and Al for O, the oxides can precipitate from the liquid during the L-DED processing. Because of the fast cooling rates, and

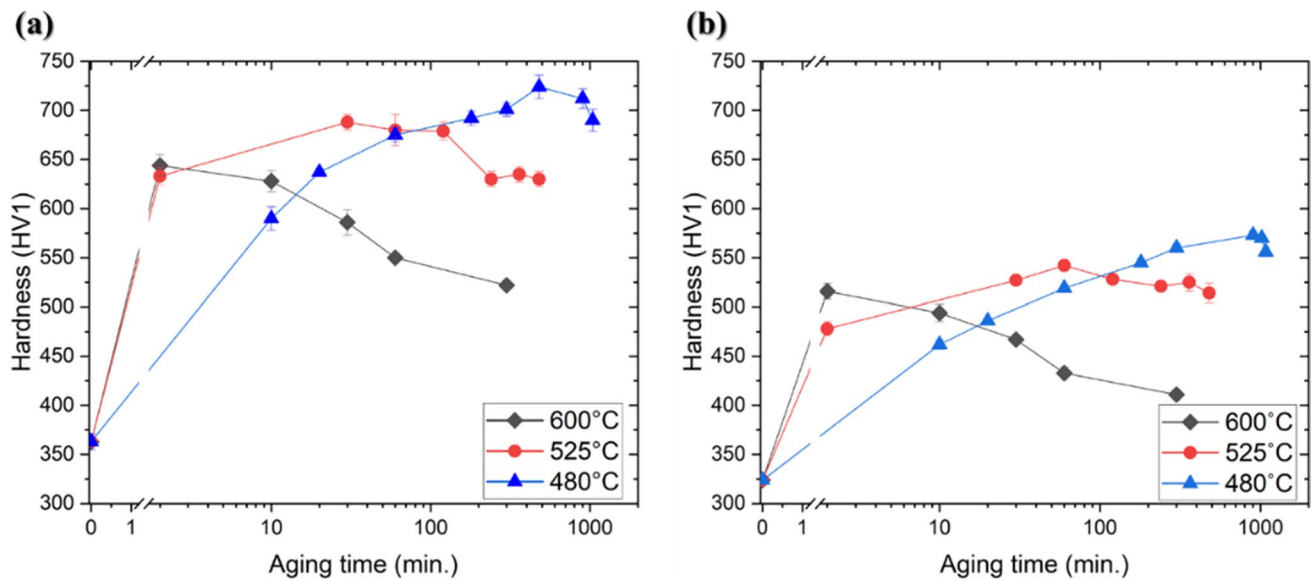


**Fig. 4** Aging curves of **a** MAR-60HRC and **b** 18Ni300 maraging steel

the constraint by primary austenite crystals, these oxides remain fine in size [51].

The aging curves (Fig. 4a) of as-built MAR-60HRC with 370 HV1 starting hardness shows that the steel (dilatometric samples) can be age-hardened in ~10 min to around 575 HV1 by aging at 480 °C. Holding for longer times (~480 min) leads to a maximum hardness of ~730 HV1. After the peak hardness is achieved (~480 min), a slight drop in hardness by longer holding is evident. By aging at 525 °C, the hardness increases to 625 HV1 in merely 2 min. Continuation of aging for 30 min results in maximum achievable hardness (680 HV1) at this aging temperature. Longer times cause softening due to over-aging. At 600 °C, the maximum hardness is obtained by 2 min holding (i.e., 650 HV1), and a longer holding time leads to overaging. For comparison, the aging curves of 18Ni300 are reported (Fig. 4b). The as-built hardness is around 330HV1, slightly lower than that of MAR-60HRC. The aging response is very similar to the MAR-60HRC, while the achievable hardness is almost 180 HV1 lower than that of the MAR-60HRC undergoing identical heat treatment schedules.

The yield strength ( $\sigma_y$ ) and hardness of maraging steel in the as-built condition can be modeled by Eq. 2 [52]

$$\sigma_y \cong 3HV \cong \sigma_0 + \sigma_{\text{martensite}} + \sigma_{ss} \quad (2)$$

where  $\sigma_0$  is the lattice friction stress,  $\sigma_{\text{martensite}}$  is the contribution of martensite sub-structure (e.g., block and lath size and dislocation density), while  $\sigma_{ss}$  represents the contribution of solid solution hardening (Eq. 3).

$$\sigma_{ss} = \sum_i \sqrt{B_i^2 x_{i,\alpha'}} \quad (3)$$

The critical resolved-shear stress due to the presence of substitutional solute atoms,  $\sigma_{ss}$ , is a function of the atomic fraction of each substitutional element ( $x_{i,\alpha'}$ ) and its strengthening constant ( $B_i$ ) given the lattice and modulus misfit compared with Fe. It is assumed that softer intercellular RA does not negatively influence the overall strength of the as-built material.

In aged conditions, intermetallic particle strengthening ( $\sigma_p$ ) emerges, which can be modeled by Orowan strengthening (Eq. 4). This term can be added linearly to Eq. 2

$$\sigma_p = 0.1\mu b \frac{f_p^{0.5}}{r_p} \ln\left(\frac{r_p}{b}\right) \quad (4)$$

where  $\mu$  is the shear modulus,  $b$  is the Burgers vector,  $f_p$  is the volume fraction of each intermetallic precipitate, and  $r_p$  is their average radius. It should be noted that after aging, the solid solution hardening effect of the elements contributing to the formation of the precipitates (i.e., Ni, Ti, and Mo) decreases by increasing the volume fraction of the precipitates.

Given the above description, especially the Orowan strengthening mechanism, up to the peak aging condition, strength increases by an increase in the number density of nano-sized precipitates, which is correlated to the vol% and size of precipitates. Over-aging leads to a drop in hardness and strength because of precipitate coarsening (i.e., lowered number density) and the formation of reverted austenite. Higher temperature aging and longer

times contribute to enhanced coarsening and a larger volume fraction of reverted austenite due to the enhanced diffusivity.

This is clearly reported that the increase in Ni content from 11 to 23 wt% does not dramatically change the dislocation density and strength of Fe–Ni lath martensite [53]. Therefore, from the strength point of view, the key difference between MAR-60HRC and 18Ni300 chemistry is their Co, Mo, and Ti content. Given the high supersaturation of alloying elements within the Fe–Ni martensite in AM-processed maraging steels, the higher as-built hardness of MAR-60HRC should be discussed in view of a larger substitutional solution hardening effect. According to Fleischer [54], the strengthening results from elastic interactions of solute atoms with screw dislocations, governed by the difference in effective modulus and size of the substituted atom. Ti and Mo show the highest solid solution strengthening effect [52], while Co (having a nearly similar atomic size to

iron) has the lowest contribution. The substantial increase in Mo causes more extensive solid solution strengthening in MAR-60HRC, leading to increased as-built hardness. Consequently, in aged condition, higher Mo wt%, and its combination with high Co gives rise to a higher vol% of  $\text{Ni}_3\text{Mo}$  and possibly  $\mu$ -phase precipitates, thus resulting in higher maximum post-age hardness (61HRC) compared with 18Ni300 (55HRC), as discussed in the previous works of authors [30].

Figure 5a and b present the microstructure of samples after aging for 5 h at 480 and 525 °C, respectively. The inset in Fig. 5a shows the uniform distribution of nano-sized intermetallic particles within the martensitic matrix, which are responsible for the increase in hardness and strength. It can be clearly observed that the thickness of the cell boundaries, which appear brighter in electron backscatter mode (BED) micrographs, is increased in the sample aged at a higher temperature. This is an indication of increased

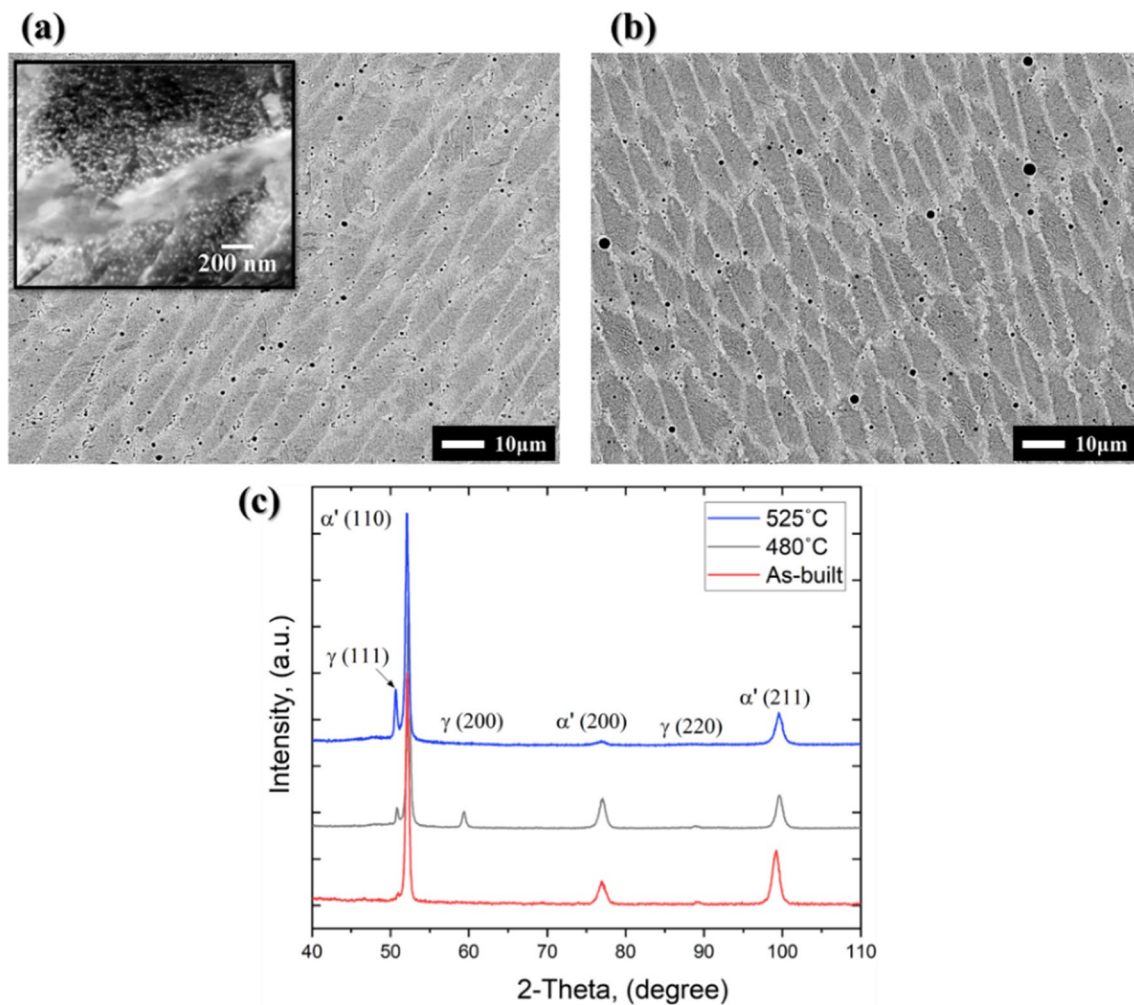


**Fig. 5** SEM micrographs L-DED MAR-60HRC aged for 5 h at **a** 480 °C (the inset highlights nano-sized precipitates within the martensitic matrix) and **b** 525 °C; note the increased thickness of the intercellular austenite appear brighter in BED-SEM micrograph; **c** XRD results



reverted austenite content upon aging at higher temperatures. In agreement with previous works [6, 55], RA at the cell boundaries can serve as a preferential site for the austenite reversion during aging. This is because, from an energetic and crystallographic point of view, it is favorable for reverted austenite to form Ni-enriched shells around existing retained austenite. In general, since austenite is an equilibrium phase in the aging temperature interval for most of the Fe–Ni maraging alloys, austenite reversion by diffusion during aging is expected. Austenite reversion is accelerated by increasing the aging temperature due to the enhanced diffusivity, leading to the local enrichment of Ni within the martensitic matrix upon dissolution of Ni-rich intermetallic precipitates and formation of Fe-Mo rich precipitates [23]. The XRD results (Fig. 5c) for the as-built samples and those aged at 480 °C and 525 °C show ~5, 8, and 20 vol% austenite, respectively. The austenite reversion kinetics at lower aging temperature for a holding time of 5 h was not significant, and the austenite content did not change drastically compared with the as-built material. Aging at higher temperatures gave rise to the reversion of a significant amount of austenite, in line with the microstructural analysis (5 a, and b) and the hardness results (Fig. 4a). The peaks pertaining to austenite in XRD measurements, especially for the sample aged at 480 °C (see (200) peak intensity), 525 °C (see (111) peak intensity), indicate the existence of a texture. The texture in RA in laser-processed steels is a result of the epitaxial growth of parent austenite at high temperature

along the build direction during the deposition (see Fig. 3). The reverted austenite preferentially grows on the existing RA and therefore preserves the same texture [56].

### 3.2 MAR-60HRC-18Ni300 Bimetal

#### 3.2.1 Interface Characteristics

An epitaxial dendrite growth can be observed in the first layer of MAR-60HRC deposited on the 18Ni300, implying a defect-free and compatible interface between the two materials due to their similar composition (Fig. 6a).

The change in the chemical composition, starting from the 18Ni300 core and passing through the interface towards MAR-60HRC at the top surface is plotted by using EDS analysis (see Fig. 6b and Table 3). The plot shows a drop

**Table 3** Composition of different layers near the interface of the bimetal, wt%

Zone/ Elements	Ni	Co	Mo	Ti	Fe
18Ni300	18.2	9.7	4.6	0.8	bal.
A1	15.5	11.8	6.4	0.6	bal.
A2	14.0	13.4	7.3	0.5	bal.
A3	13.3	14.0	8.3	0.4	bal.
MAR-60HRC	12.7	15.0	9.0	0.3	bal.
50%-50% nominal mix	15.5	12.2	7.3	0.5	bal.

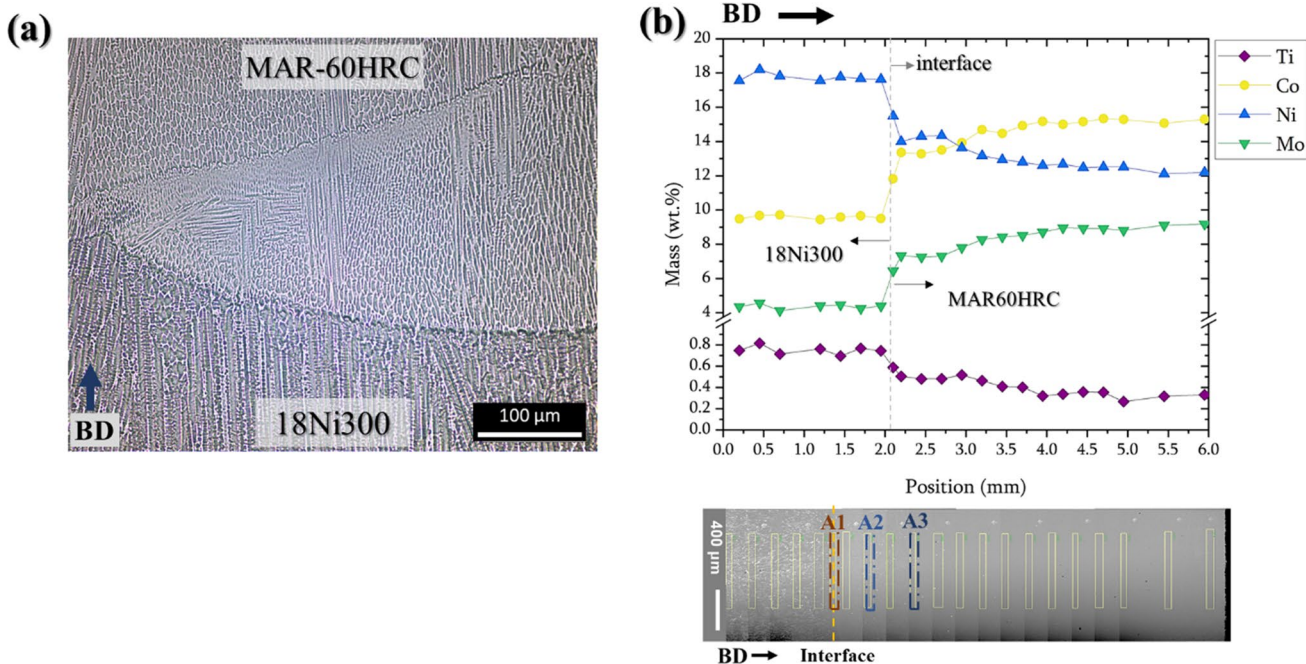


**Fig. 6** a LOM micrograph showing the interface in as-deposited bimetal, b EDS analysis results for Ti, Co, Ni, and Mo along the height and the corresponding SEM micrograph of the interface between the two materials



in Ni and Ti wt% to ~15.5 and 0.6 respectively in the first deposited layer of MAR-60HRC at the interface, while Mo and Co increase significantly to around 6.4 and 12.0 wt% respectively (zone A1, Fig. 6b and Table 3). By approaching the second layer of MAR-60HRC, Ni content further decreases to ~14.0 wt%, and Ti to ~0.5 wt%, while Mo and Co increase to 7.3 and 14.0 wt%, respectively (zone A2, Fig. 6b and Table 3). Within the third layer of the deposited MAR-60HRC, the concentration profiles become relatively flat, and the chemical composition detected by EDS approaches the nominal MAR-60HRC composition (zone A3, Fig. 6b and Table 3). For comparison, the theoretical chemical composition in the case of mixing the two powders at equal wt% (i.e., 50/50) is shown in Table 3. The results indicate that a mixture of 18Ni300 and MAR-60HRC characterizes the vicinity of the interface, showing an equivalent chemical composition in between the starting materials, which can be roughly said to comprise ~50 wt% 18Ni300, MAR-60HRC bal. By increasing the distance from the interface, the material gradually is diluted in 18Ni300 and approaches the pure MAR-60HRC composition. This is achieved roughly at the top surface of the third deposited layer of MAR-60HRC onwards.

With reference to a previous work of the authors on the simulation of the thermal histories of the deposited layers using current processing parameters [30], it is plausible that by the deposition of the first layer of MAR-60HRC, the last

deposited layer of 18Ni300 partially remelts and mixing of these materials takes places in the liquid state due to Marangoni effect. This should probably lead to a composition that roughly contains 50 wt% 18Ni300, and 50 wt% MAR-60HRC at the vicinity of the interface (i.e., mixed layer 1, corresponding to regions in the 1st deposited layer of MAR-60HRC). By depositing the second layer of MAR-60HRC, the solidified layer (mixed layer 1) is partially remelted and mixed with the MAR-60HRC, and the equivalent solidified composition may become roughly 25wt% 18Ni300, and 75wt% MAR-60HRC (i.e., mixed layer 2). The successive depositions probably result in a highly diluted composition in 18Ni300, which can be considered pure MAR-60HRC. Moreover, due to the heat transfer from the solidifying layers to the solidified layers, the concentration gradients might lead to interdiffusion at high temperatures in the solid state. This discussion is essential as it will be used later in this manuscript to describe the hardness profile of the bimetal. Given the compatible chemical compositions of the two alloys, the smooth concentration profiles of the alloying elements near the interface, and the SEM micrographs, no parasitic reaction phases at the interface are expected.

The hardness profiles (Fig. 7a) before and after the age hardening of the bimetal confirm that the as-built hardness of the 18Ni300 is around 325 HV. By approaching the interface, the hardness increases to about 340 HV and rises gradually to around 370 HV in the MAR-60HRC region, in

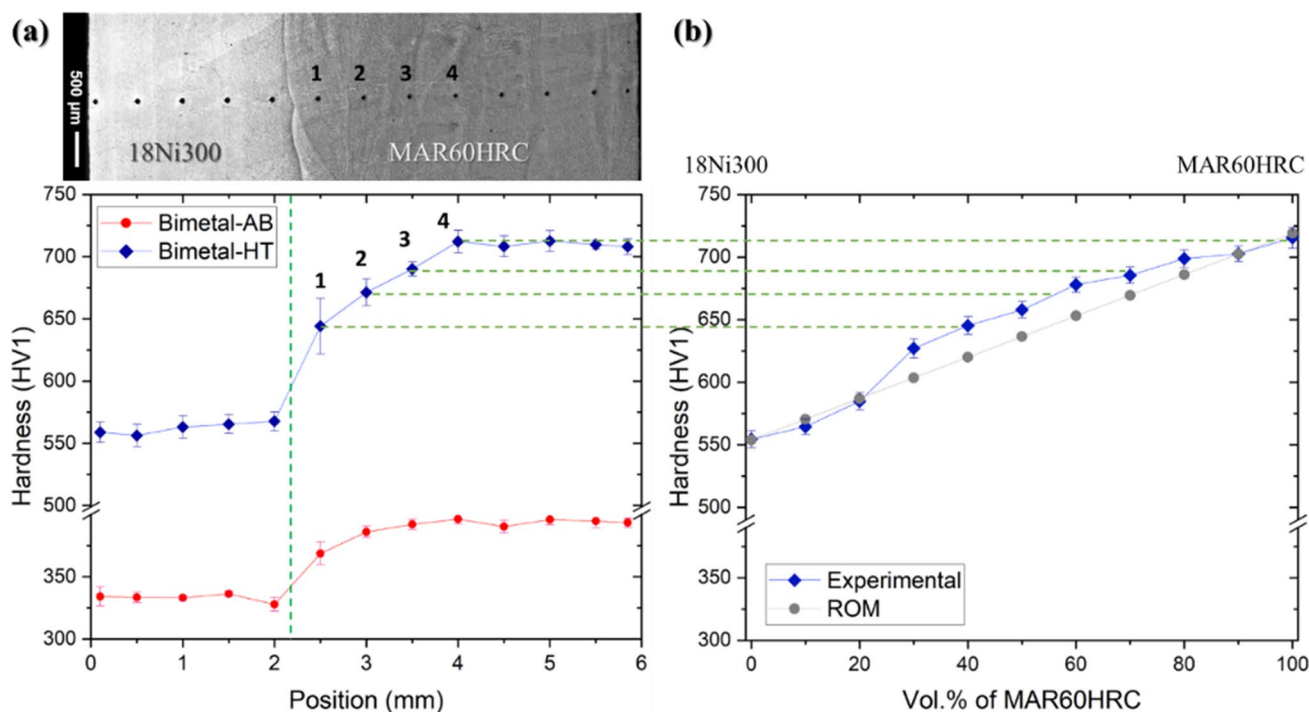


**Fig. 7** **a** Hardness profile across the height for the bimetal samples in the as-built and aged states, **b** Hardness profile of the CG sample experimental and ROM

line with the aging curves of the two base materials (Fig. 4). In the aged condition, a similar trend is observed. Hardness in 18Ni300 is around 560 HV and increases to 650 HV at the interface, followed by a gradual increase to  $\sim 720$  HV. The hardness gradient at the interface covers around 2 mm, roughly representative of three deposited layers (layer thickness  $\sim 0.7$  mm), which is in agreement with the chemical composition gradient near the interface, where mixing of the softer 18Ni300 with MAR-60HRC was evident. In order to further investigate the dilution influence on the hardness, a compositionally graded (CG) sample was produced through an in-situ mixture of powders and by increasing the amount of MAR-60HRC by 10 vol% in each successive layer. The experimental hardness profile and the calculated hardness profile based on the rule of mixture (ROM) are depicted in Fig. 7b. The microhardness at point 1 in Fig. 8a is equal to the microhardness of the layer with 40 vol% of MAR-60HRC in Fig. 8b. In the second layer, covering points 2, and 3 in Fig. 8a, the microhardness in bimetal lies in between of the hardness levels of 60 to 70 vol% of MAR-60HRC (see Fig. 7b). At the top of the third deposited layer (point 4 in Fig. 8a), the microhardness approaches that of 100% MAR-60HRC (see Fig. 7b). The microhardness does not change further from point 4 towards the top layers of the bimetal, therefore, still corresponding to the hardness of pure MAR-60HRC. Together with the EDS analysis, these results can appropriately explain the interface characteristics. The discrepancy between the ROM and experimental results can be due to the change in precipitation kinetics by changing Mo, Ti, and Co content in the mixtures. In 18Ni300 with 0.6–0.8 wt% Ti,  $\text{Ni}_3\text{Ti}$  is one of the main precipitates to form at 400 °C to 500 °C aging interval; this is accompanied by the

precipitation of Mo-rich intermetallic particles (e.g.,  $\text{Ni}_3\text{Mo}$ ) [57]. By increasing Mo and decreasing Ti in the mixtures, which comprise higher vol% of MAR-60HRC, the activity of Mo increases; moreover, the increase in Co wt% decreases the solubility of Mo in the matrix. The combination of these two factors enhances the precipitation of the  $\text{Ni}_3\text{Mo}$ , while  $\text{Ni}_3\text{Ti}$  will still be present as a result of the higher Ti content in the mixtures compared with the pure MAR-60HRC. The morphology and size of these two precipitates at the aging temperature differ from each other [12], leading to different contributions to strength according to the Orowan relation. This can lead to an increased experimental hardness compared with the theoretical ROM results. Interestingly, when the vol% of MAR-60HRC in the mixture is either low (i.e., up to 20%) or high (i.e., 90%), the experimental hardness is identical to that of ROM; therefore, there exists a threshold above which, the precipitation kinetics will be affected by the introduction of the second material. This needs to be further analyzed in the future work of the authors using thermal analysis.

### 3.2.2 Fracture Toughness

The  $K_{\text{app}}$  of the 18Ni300 at  $565 \pm 6$  HV is  $90 \pm 2$  MPa  $\text{m}^{1/2}$ , and this value drops to  $60 \pm 3$  MPa  $\text{m}^{1/2}$  for MAR-60HRC at  $725 \pm 8$  HV. The Bimetal specimen shows a fracture toughness of  $71 \pm 2$  MPa  $\text{m}^{1/2}$  at a similar surface hardness level of MAR-60HRC (Fig. 8a). It can be clearly observed that the  $K_{\text{app}}$  values are systematically higher than the  $K_{\text{IC}}$  for the wrought samples, which can be attributed both to the microstructure of AM samples as well as the effect of the blunt notch on the stress field at notch tip for the

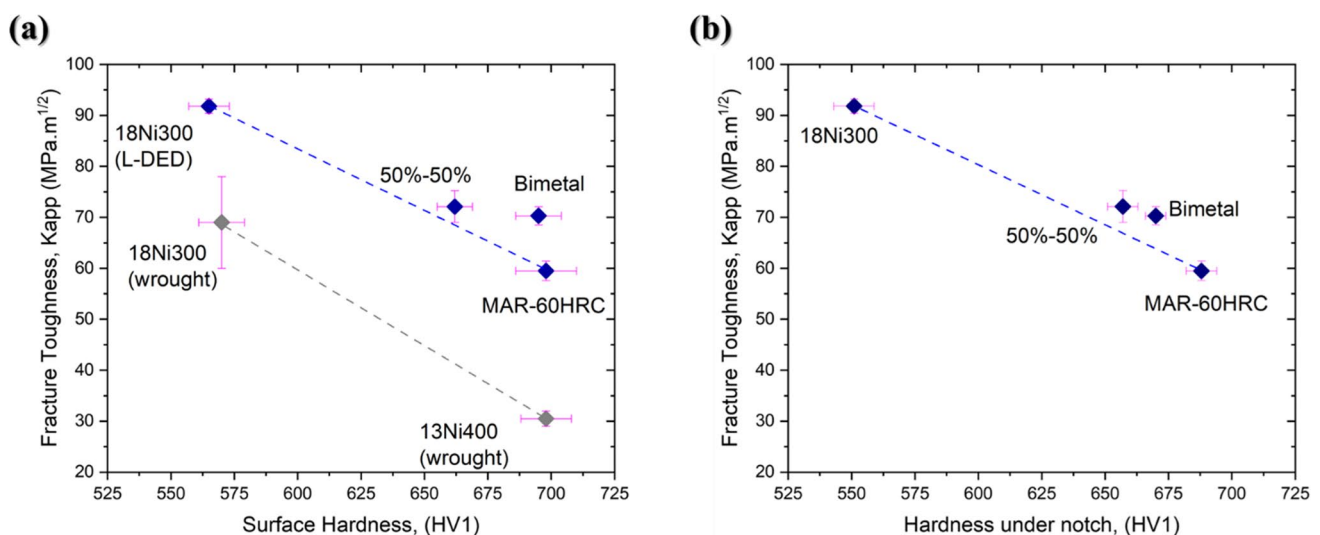


**Fig. 8** Apparent fracture toughness values for the samples versus surface hardness (blue points), as well as  $K_{\text{IC}}$  for wrought 18Ni300 [59, 60] and 13Ni400 [19, 48] (gray points), and **b**  $K_{\text{app}}$  versus hardness under the notch for L-DED specimens

samples in the current study. The higher toughness of bimetal compared with MAR-60HRC can be attributed to the influence of concentration and hardness gradient near the interface. The notch tip was located in an area showing a hardness of  $\sim 670\text{HV}$  (Fig. 8b), which is equal to the hardness of a mixture of 50% MAR-60HRC, 18Ni300 bal. (see Figs. 6 and 7). The lower hardness below the notch leads to higher  $K_{\text{app}}$  in bimetal. In order to confirm this hypothesis, fracture toughness tests were carried out on samples processed by the 50%-50% mixtures of MAR-60HRC and 18Ni300. The fracture toughness of the 50%-50% samples, showing a hardness level of 660 HV, perfectly lies in between 18Ni300 and MAR-60HRC (Fig. 8a) and matches with that of bimetal if hardness under notch is taken into account for the latter (Fig. 8b). It is evident that the bimetal with a very high surface hardness shows an excellent fracture toughness as well, shifting its position to the right side of the hardness-toughness linear trend. This is mainly due to a defect-free interface

and the concentration and hardness gradients below the notch. The fracture toughness obtained in this work for 18Ni300 and MAR-60HRC are systematically higher than those of conventionally manufactured maraging counterparts at the same hardness level (see Fig. 1). As discussed earlier in the experimental section, this is a consequence of the larger notch tip radius in the current study compared with the fatigue pre-cracked notch. This systematic difference was also documented in other works [58], where the fracture toughness of the tool steels by using a fatigue pre-cracked notch (i.e.,  $\rho \rightarrow 0$ ) was lower than those performed on the EDM notched samples with a notch radius of 50  $\mu\text{m}$ .

The fracture surface of 18Ni300 shows ductile transgranular fracture with the presence of dimples (Fig. 9a and b). This can be considered a completely transgranular fracture. The fracture surface of the MAR-60HRC, on the other hand, shows a quasi-cleavage fracture behavior, a preferential crack propagation along the columnar grains and dendritic substructure can be observed, but it is hard

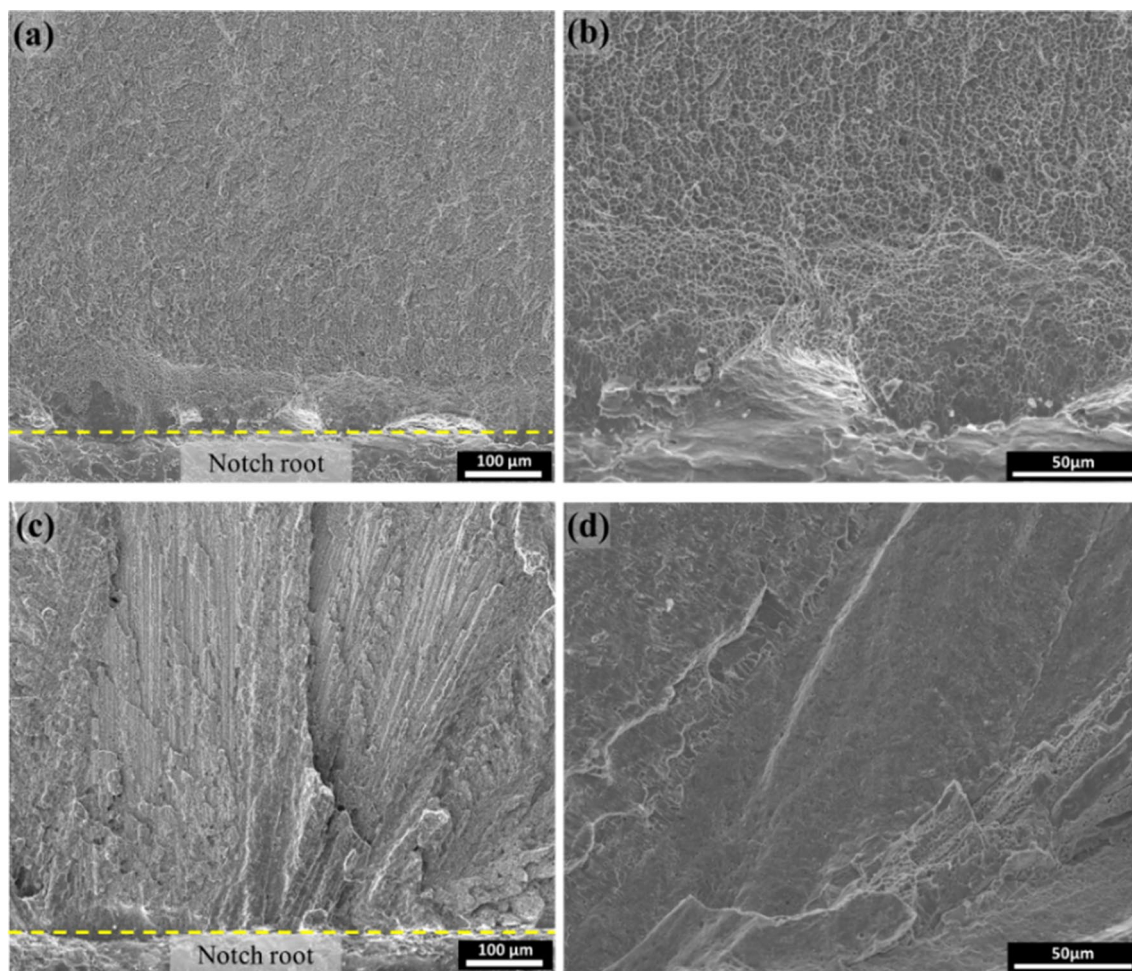


**Fig. 9** SEM images of the fracture surfaces for **a&b** 18Ni300 and **c&d** MAR-60HRC



to be concluded as an intergranular fracture (Fig. 9c, and d). The crack interaction with the interface in the bimetal sample will be discussed in the next section.

### 3.2.3 Crack Interaction with Interface in Bimetal

The load–displacement curves in 18Ni300 show that after reaching the maximum force (i.e., the onset of crack initiation), the load drops instantaneously due to the unstable crack propagation until complete fracture (Fig. 10a). Signs of limited plastic deformation before reaching the maximum load were evident in the load–displacement records. However, drawing the 5% secant line following the ASTM E399 recommendation did not result in a significant change in the fracture toughness calculations. The records for the MAR-60HRC is also showing a similar sudden load drop after reaching the maximum load, and the load–displacement curve obeys a perfect linear elastic behavior (Fig. 10a).

The load–displacement record in bimetal is different, and it shows a maximum, followed by a sudden drop to around 0.4 kN, representing the unstable crack propagation up to that point (Fig. 10a) and not reaching zero without showing a complete fracture. At this point, to further understand the crack propagation behavior, the test was conducted for one sample with sustained loading until complete fracture (Fig. 10b). Looking at the load–displacement curve, the appearance of a pop-in is obvious (inset in Fig. 10b), where the force slightly increases after the sudden drop and again starts to decrease gradually until complete fracture. This behavior can be related to a decline in the driving force for crack propagation and crack arrest in the microstructure. Thus a larger driving force was needed for the crack propagation.

Interestingly, the metallographic cross-section prepared after stopping the test before the occurrence of the pop-in shows that the propagating crack in the MAR-60HRC region is arrested at the interface due to the shielding effect of the tougher 18Ni300 (Fig. 11a) in agreement with the load–displacement curve. The crack propagation path in bi-material layered structures is governed by a competition between the direction of the "maximum" driving force and the "weakest" microstructural path [59]. This experiment shows that the original crack, "perpendicular" to the interface, does not deflect towards the interface when approaching it. Therefore, the interface was not the "weakest" path. This can be another indication of a strong and defect-free interface, thanks to the very compatible chemical composition of the two materials which implies a good bonding between the hard surface and the tough core that can preclude delamination or spalling specifically in tooling application. Moreover, by continuing the loading, the crack propagates in the 18Ni300, and the fracture surface at the interface shows a transition from a quasi-cleavage fracture in MAR-60HRC to a transgranular ductile fracture in 18Ni300 with no traces of decohesion or transversal cracking at the interface (Fig. 11b). This is also backed by the EDS analysis on Area 1 (The first deposited layer of MAR-60HRC) and Area 2 (18Ni300) in the vicinity of the interface (Table 4). Apart from the improved  $K_{app}$  of bimetal compared with MAR-60HRC, the crack arrest at the interface (i.e., extrinsic toughening effect) can account for an increased damage tolerance factor in industrial applications. It is noteworthy that the scope of the current study was mainly to demonstrate the feasibility of improving fracture toughness through the fabrication of bimetal parts and to verify the possibility of stopping crack

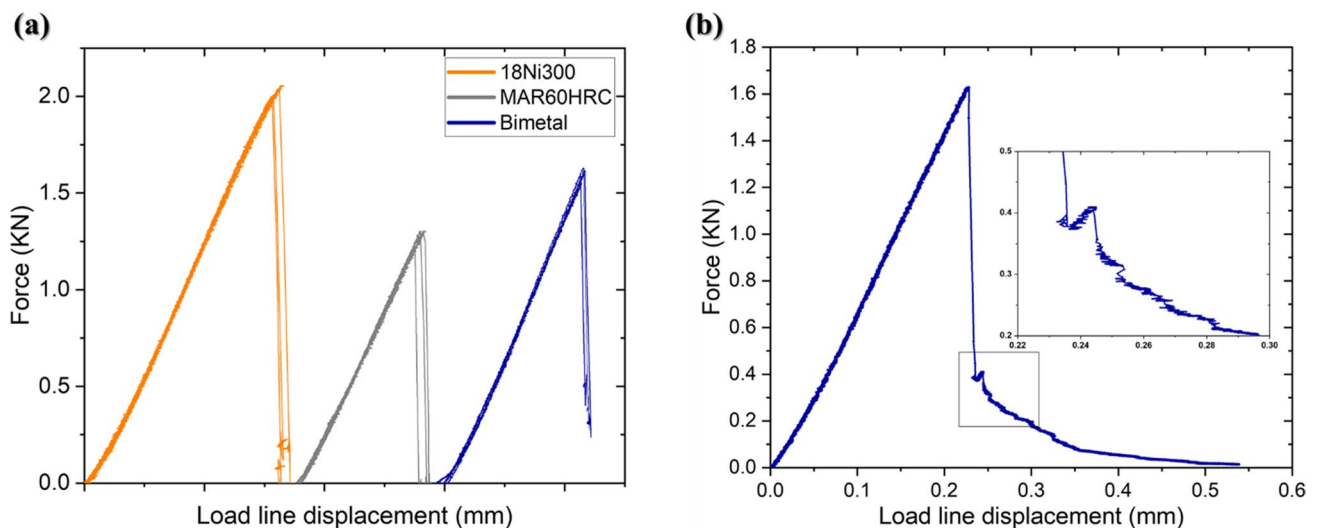


**Fig. 10** **a** Load displacement curves for the fracture toughness tests and **b** load pop-in for the bimetal

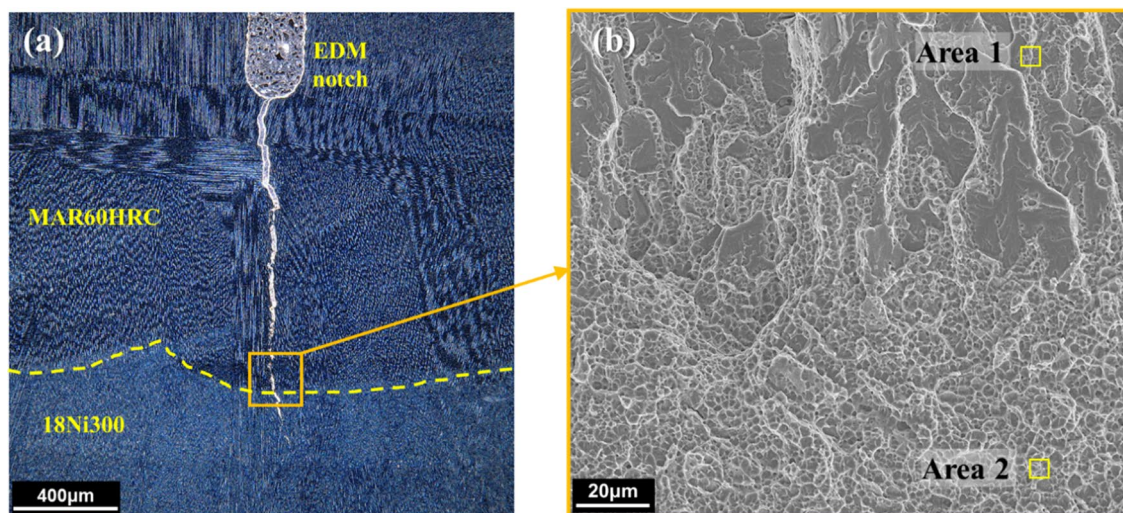


**Fig. 11** **a** DF-LOM image highlighting the crack propagation path in the bimetal samples, and **b** SEM image of the fracture at the interface of the two materials, demonstrating the transition of fracture mode

**Table 4** Chemical composition of two areas at the fracture interface of the bimetal, in wt%

Element	Fe	Ni	Co	Mo	Ti
Area 1	64.7	13.7	13.5	7.8	0.4
Area 2	64.1	18.1	9.9	5.3	0.9

propagation thanks to the softer substrate and the effect of notch configuration, notch length and thickness of the hard layer on the fracture toughness is subject of another ongoing study.

## 4 Conclusion

A modified ultrahigh strength maraging steel (MAR-60HRC) was fabricated using laser metal deposition, and subsequently, the possibility of producing bimetals with a hard surface (MAR-60HRC) and a tougher core (18Ni300) was evaluated. From the experimental work carried out in this work, the following conclusions can be drawn:

- As-built microstructure of MAR-60HRC comprised martensite and a small vol% of intercellular retained austenite because of heavy micro-segregation of alloying elements to the cellular boundaries.
- Direct aging at 480 °C for 6 h resulted in a high hardness (~720 HV) for the MAR-60HRC, about 180 HV higher than reference 18Ni300. Aging at higher temperatures resulted in earlier hardness drop due to austenite reversion and precipitate coarsening.

- The fracture toughness ( $K_{app}$ ) of MAR-60HRC at the peak aged condition was lower than that of 18Ni300 (i.e., 60 MPa m<sup>1/2</sup> vs. 90 MPa m<sup>1/2</sup>).
- Bimetal samples composed of a high-toughness core of 18Ni300 and a hard surface of MAR-60HRC were deposited successfully. A smooth microstructural and hardness transition could be observed without evident interface defects. The fracture toughness ( $K_{app}$ ) of the bimetal (i.e., 71 MPa m<sup>1/2</sup>) was higher than that of MAR-60HRC and lower than 18Ni300. While the surface hardness of the bimetal was equal to that of MAR-60HRC (~720 HV).
- The fracture toughness results in the current work are systematically higher than the  $K_{IC}$  reported in literature for the wrought counterparts, which is mainly due to the effect of the blunt notch on the stress field at notch tip for the samples in the current study.
- In addition to the enhanced fracture toughness, the bimetal with a hard surface and a softer core exhibited crack arrest at the interface. This extrinsic toughening effect can be of high interest when designing a high wear resistant, and damage-tolerant material.

**Acknowledgements** Two of the authors (SA and PB) acknowledge the financial support from the AMICO project (Grant number ARS01\_00758) from the Italian Ministry of Education.

**Funding** Open access funding provided by Università degli Studi di Trento within the CRUI-CARE Agreement.

## Declarations

**Conflict of interest** On behalf of all authors, the corresponding author states that there is no conflict of interest.

**Open Access** This article is licensed under a Creative Commons Attribution 4.0 International License, which permits use, sharing, adaptation, distribution and reproduction in any medium or format, as long as you give appropriate credit to the original author(s) and the source, provide a link to the Creative Commons licence, and indicate if changes were made. The images or other third party material in this article are included in the article's Creative Commons licence, unless indicated otherwise in a credit line to the material. If material is not included in the article's Creative Commons licence and your intended use is not permitted by statutory regulation or exceeds the permitted use, you will need to obtain permission directly from the copyright holder. To view a copy of this licence, visit <http://creativecommons.org/licenses/by/4.0/>.

## References

1. P. Bajaj, A. Hariharan, A. Kini, P. Kürnsteiner, D. Raabe, E.A. Jäggle, Steels in additive manufacturing: a review of their microstructure and properties. *Manuf. Sci. Eng. A* **772**, 138633 (2020). <https://doi.org/10.1016/j.msea.2019.138633>
2. N. Haghdad, M. Laleh, M. Moyle, S. Primig, Additive manufacturing of steels: a review of achievements and challenges. *J. Mater. Sci.* **56**(1), 64–107 (2021). <https://doi.org/10.1007/s10853-020-05109-0>
3. S. Ford, M. Despeisse, Additive manufacturing and sustainability: an exploratory study of the advantages and challenges. *J. Clean. Prod.* **137**, 1573–1587 (2016). <https://doi.org/10.1016/j.jclepro.2016.04.150>
4. D.-G. Ahn, Directed energy deposition (DED) Process: State of the Art, *Int. J. Precis. Eng. Manuf.-Green Tech.* **8**, (2), 703–742, 2021. <https://doi.org/10.1007/s40684-020-00302-7>
5. H. Knoll, S. Ocylok, A. Weisheit, H. Springer, E. Jäggle, D. Raabe, Combinatorial alloy design by laser additive manufacturing. *Steel Res. Int.* **88**(8), 1600416 (2017)
6. E.A. Jäggle, P.-P. Choi, J. Van Humbeeck, D. Raabe, Precipitation and austenite reversion behavior of a maraging steel produced by selective laser melting. *J. Mater. Res.* **29**(17), 2072–2079 (2014). <https://doi.org/10.1557/jmr.2014.204>
7. Z. Guo, W. Sha, Modelling the correlation between processing parameters and properties of maraging steels using artificial neural network. *Comput. Mater. Sci.* **29**(1), 12–28 (2004). [https://doi.org/10.1016/S0927-0256\(03\)00092-2](https://doi.org/10.1016/S0927-0256(03)00092-2)
8. A. Magnee, J.M. Drapier, J. Dumont, D. Coutsouradis, L. Habrakan, Cobalt-containing high-strength steels, INIS-MF--1971 (Centre d'Information du Cobalt, Brussels, 1974). Available: [http://inis.iaea.org/Search/search.aspx?orig\\_q=RN:6217555](http://inis.iaea.org/Search/search.aspx?orig_q=RN:6217555)
9. W. Sha, A. Cerezo, G.D.W. Smith, Phase chemistry and precipitation reactions in maraging steels: Part IV. Discussion and conclusions. *Metall. Mater. Trans. A* **24**(6), 1251–1256 (1993). <https://doi.org/10.1007/BF02668193>
10. W. Sha, Thermodynamic calculations for precipitation in maraging steels. *Mater. Sci. Technol.* **16**(11–12), 1434–1436 (2000). <https://doi.org/10.1179/026708300101507415>
11. W.W. Sun, R.K.W. Marceau, M.J. Styles, D. Barbier, C.R. Hutchinson, G phase precipitation and strengthening in ultra-high strength ferritic steels: towards lean ‘maraging’ metallurgy. *Acta Mater.* **130**, 28–46 (2017). <https://doi.org/10.1016/j.actamat.2017.03.032>
12. O. Moshka, M. Pinkas, E. Brosh, V. Ezersky, L. Meshi, Addressing the issue of precipitates in maraging steels – Unambiguous answer. *Mater. Sci. Eng. A* **638**, 232–239 (2015). <https://doi.org/10.1016/j.msea.2015.04.067>
13. S. Bodziak, K.S. Al-Rubaie, L. Dalla Valentina, F.H. Lafratta, E.C. Santos, A.M. Zanatta, Y. Chen, Precipitation in 300 grade maraging steel built by selective laser melting: Aging at 510 °C for 2 h. *Mater. Charact.* **151**, 73–83 (2019). <https://doi.org/10.1016/j.matchar.2019.02.033>
14. A.M. Hall, C.J. Slunder, *The Metallurgy, Behavior, and Application of the 18-Percent Nickel Maraging Steels*, NASA-SP-5051 (NASA, Washington, 1968). Available: <https://apps.dtic.mil/docs/citations/ADA382105>
15. D.G. Lee, K.C. Jang, J.M. Kuk, I.S. Kim, The influence of niobium and aging treatment in the 18% Ni maraging steel. *J. Mater. Process. Technol.* **162–163**, 342–349 (2005). <https://doi.org/10.1016/j.jmatprotec.2005.02.102>
16. H. Shirazi, G. Miyamoto, S. Hossein Nedjad, T. Chiba, M. Nili Ahmadabadi, T. Furuahara, Microstructure evolution during austenite reversion in Fe-Ni martensitic alloys. *Acta Mater.* **144**, 269–280 (2018). <https://doi.org/10.1016/j.actamat.2017.10.068>
17. A. Fathy, T. Mattar, H. El-Faramawy, W. Bleck, Mechanical properties of new low-nickel cobalt-free maraging steels. *Steel Res.* **73**(12), 549–556 (2002). <https://doi.org/10.1002/srin.200200027>
18. L. Sun, T.H. Simm, T.L. Martin, S. McAdam, D.R. Galvin, K.M. Perkins, P.A.J. Bagot, M.P. Moody, S.W. Ooi, P. Hill, M.J. Rawson, H.K.D.H. Bhadeshia, A novel ultra-high strength maraging steel with balanced ductility and creep resistance achieved by nanoscale  $\beta$ -NiAl and Laves phase precipitates. *Acta Mater.* **149**, 285–301 (2018). <https://doi.org/10.1016/j.actamat.2018.02.044>
19. Y. He, K. Yang, W. Qu, F. Kong, G. Su, Strengthening and toughening of a 2800-MPa grade maraging steel. *Mater. Lett.* **56**(5), 763–769 (2002). [https://doi.org/10.1016/S0167-577X\(02\)00610-9](https://doi.org/10.1016/S0167-577X(02)00610-9)
20. Y. He, K. Yang, W. Sha, Microstructure and mechanical properties of a 2000 MPa grade co-free maraging steel. *Metall. Mater. Trans. A* **36**(9), 2273–2287 (2005). <https://doi.org/10.1007/s11661-005-0100-9>
21. J. Grum, M. Zupančič, Behaviour of 12% Ni steel with the change of initial precipitates. *J. Mater. Process. Technol.* **155–156**, 2019–2025 (2004). <https://doi.org/10.1016/j.jmatprotec.2004.04.305>
22. V.K. Vasudevan, S.J. Kim, C.M. Wayman, Precipitation reactions and strengthening behavior in 18 Wt Pct nickel maraging steels. *Metall. Trans. A* **21**(10), 2655–2668 (1990). <https://doi.org/10.1007/BF02646061>
23. S. Floreen, The physical metallurgy of maraging steels. *Metall. Rev.* **13**(1), 115–128 (1968). <https://doi.org/10.1179/mtr.1968.13.1.115>
24. L.F. Van Swam, R.M. Pelloux, N.J. Grant, Fatigue behavior of maraging steel 300. *Metall. Trans. A* **6**(1), 45–54 (1975). <https://doi.org/10.1007/BF02673669>
25. B.-Z. Weiss, Maraging steels—structure, properties and applications, in *Specialty Steels and Hard Materials*, ed. by N.R. Comins, J.B. Clark (Pergamon, Oxford, 1983), pp. 35–54. <https://doi.org/10.1016/B978-0-08-029358-5.50009-4>
26. J. Suryawanshi, K.G. Prashanth, U. Ramamurty, Tensile, fracture, and fatigue crack growth properties of a 3D printed maraging steel through selective laser melting. *J. Alloys Compd.* **725**, 355–364 (2017). <https://doi.org/10.1016/j.jallcom.2017.07.177>
27. P.L.L. Santos, J.A. Avila, E.B. da Fonseca, A.H.G. Gabriel, A.L. Jardini, É.S.N. Lopes, Plane-strain fracture toughness of thin additively manufactured maraging steel samples. *Addit. Manuf.* **49**, 102509 (2022). <https://doi.org/10.1016/j.addma.2021.102509>
28. J. Hunt, F. Derguti, I. Todd, Selection of steels suitable for additive layer manufacturing. *Ironmak. Steelmak.* **41**(4), 254–256 (2014). <https://doi.org/10.1179/0301923314Z.000000000269>
29. Metal AM Summer 2016, *Metal Additive Manufacturing*. <https://www.metal-am.com/magazine-metal-summer-2016-pdf-single-page-edition/>. Accessed 17 July 2019
30. S. Amirabdollahian, F. Deirmina, L. Harris, R. Siriki, M. Pellizzari, P. Bosetti, A. Molinari, Towards controlling intrinsic heat



- treatment of maraging steel during laser directed energy deposition. *Scr. Mater.* **201**, 113973 (2021). <https://doi.org/10.1016/j.scriptamat.2021.113973>
31. X. Yan, C. Huang, C. Chen, R. Bolot, L. Dembinski, R. Huang, W. Ma, H. Liao, M. Liu, Additive manufacturing of WC reinforced maraging steel 300 composites by cold spraying and selective laser melting. *Surf. Coat. Tech.* **371**, 161–171 (2019). <https://doi.org/10.1016/j.surfcoat.2018.03.072>
  32. J. Hu, H. Zhu, J. Zhang, M. Ouyang, C. Qiu, J. Duan, Effects of TiC addition on microstructure, microhardness and wear resistance of 18Ni300 maraging steel by direct laser deposition. *J. Mater. Process. Tech.* **296**, 117213 (2021). <https://doi.org/10.1016/j.jmatprotec.2021.117213>
  33. Z. Li, B. Teng, B. Yao, J. Liu, Microstructure and mechanical properties of WC reinforced 18Ni300 composites produced by selective laser melting. *Mater. Charact.* **180**, 111406 (2021). <https://doi.org/10.1016/j.matchar.2021.111406>
  34. N. Kang, W. Ma, L. Heraud, M. El Mansori, F. Li, M. Liu, H. Liao, Selective laser melting of tungsten carbide reinforced maraging steel composite. *Addit. Manuf.* **22**, 104–110 (2018). <https://doi.org/10.1016/j.addma.2018.04.031>
  35. K. Shetty, S. Kumar, P. Raghobhama Rao, Effect of ion nitriding on the microstructure and properties of maraging steel (250 Grade). *Surf. Coat. Tech.* **203**, 1530–1536 (2009). <https://doi.org/10.1016/j.surfcoat.2008.11.034>
  36. Y. Hong, D.D. Dong, S.S. Lin, W. Wang, C.M. Tang, T.C. Kuang, M.J. Dai, Improving surface mechanical properties of the selective laser melted 18Ni300 maraging steel via plasma nitriding. *Surf. Coat. Tech.* **406**, 126675 (2021). <https://doi.org/10.1016/j.surfcoat.2020.126675>
  37. M. Godec, B. Podgornik, A. Kocijan, Č. Donik, D.A.S. Balantič, Use of plasma nitriding to improve the wear and corrosion resistance of 18Ni-300 maraging steel manufactured by selective laser melting. *Sci. Rep.* **11**(1), 3277 (2021). <https://doi.org/10.1038/s41598-021-82572-y>
  38. S. Shakerin, M. Sanjari, B.S. Amirkhiz, M. Mohammadi, Interface engineering of additively manufactured maraging steel-H13 bimetallic structures. *Mater. Charact.* **170**, 110728 (2020). <https://doi.org/10.1016/j.matchar.2020.110728>
  39. S. Shakerin, A. Hadadzadeh, B.S. Amirkhiz, S. Shamsdini, J. Li, M. Mohammadi, Additive manufacturing of maraging steel-H13 bimetallics using laser powder bed fusion technique. *Addit. Manuf.* **29**, 100797 (2019). <https://doi.org/10.1016/j.addma.2019.100797>
  40. R.O. Ritchie, The conflicts between strength and toughness. *Nat. Mater.* **10**, 11 (2011). <https://doi.org/10.1038/nmat3115>
  41. R.O. Ritchie, Mechanisms of fatigue crack propagation in metals, ceramics and composites: role of crack tip shielding. *Mater. Sci. Eng. A* **103**(1), 15–28 (1988). [https://doi.org/10.1016/0025-5416\(88\)90547-2](https://doi.org/10.1016/0025-5416(88)90547-2)
  42. J. Suryawanshi, K.G. Prashanth, S. Scudino, J. Eckert, O. Prakash, U. Ramamurty, Simultaneous enhancements of strength and toughness in an Al-12Si alloy synthesized using selective laser melting. *Acta Mater.* **115**, 285–294 (2016). <https://doi.org/10.1016/j.actamat.2016.06.009>
  43. S. Huang, P. Kumar, W.Y. Yeong, R.L. Narayan, U. Ramamurty, Fracture behavior of laser powder bed fusion fabricated Ti41Nb via in-situ alloying. *Acta Mater.* **225**, 117593 (2022). <https://doi.org/10.1016/j.actamat.2021.117593>
  44. P. Kürnsteiner, M.B. Wilms, A. Weisheit, B. Gault, E.A. Jägler, D. Raabe, High-strength Damascus steel by additive manufacturing. *Nature* **582**, 515–519 (2020). <https://doi.org/10.1038/s41586-020-2409-3>
  45. B.-W. Lee, J. Jang, D. Kwon, Evaluation of fracture toughness using small notched specimens. *Mater. Sci. Eng. A* **334**(1–2), 207–214 (2002). [https://doi.org/10.1016/S0921-5093\(01\)01804-4](https://doi.org/10.1016/S0921-5093(01)01804-4)
  46. Y. Sugimura, P.G. Lim, C.F. Shih, S. Suresh, Fracture normal to a bimaterial interface: effects of plasticity on crack-tip shielding and amplification. *Acta Metall. Mater.* **43**(3), 1157–1169 (1995). [https://doi.org/10.1016/0956-7151\(94\)00295-S](https://doi.org/10.1016/0956-7151(94)00295-S)
  47. F. Deirmina, P.A. Davies, R. Casati, Effects of powder atomization route and post-processing thermal treatments on the mechanical properties and fatigue resistance of additively manufactured 18Ni300 maraging steel. *Adv. Eng. Mater.* **24**, 2101011 (2021). <https://doi.org/10.1002/adem.202101011>
  48. W. Wang, W. Yan, Q. Duan, Y. Shan, Z. Zhang, K. Yang, Study on fatigue property of a new 2.8GPa grade maraging steel. *Mater. Sci. Eng. A* **527**(13–14), 3057–3063 (2010). <https://doi.org/10.1016/j.msea.2010.02.002>
  49. Maud – Materials Analysis Using Diffraction. <http://nanoair.dii.unitn.it:8080/maud/> (Accessed 08 Dec. 2021)
  50. S. Amirabdollahian, F. Deirmina, M. Pellizzari, P. Bosetti, A. Molinari, Tempering behavior of a direct laser deposited hot work tool steel Influence of quenching on secondary hardening and microstructure. *Mater. Sci. Eng. A* **814**, 141126 (2021). <https://doi.org/10.1016/j.msea.2021.141126>
  51. F. Yan, W. Xiong, E. Faierson, G.B. Olson, Characterization of nano-scale oxides in austenitic stainless steel processed by powder bed fusion. *Scr. Mater.* **155**, 104–108 (2018). <https://doi.org/10.1016/j.scriptamat.2018.06.011>
  52. E.I. Galindo-Nava, W.M. Rainforth, P.E.J. Rivera-Díaz-del-Castillo, Predicting microstructure and strength of maraging steels: elemental optimisation. *Acta Mater.* **117**, 270–285 (2016). <https://doi.org/10.1016/j.actamat.2016.07.020>
  53. S. Morito, J. Nishikawa, T. Maki, Dislocation density within lath martensite in Fe-C and Fe-Ni alloys. *ISIJ Int.* **43**(9), 1475–1477 (2003). <https://doi.org/10.2355/isijinternational.43.1475>
  54. R.L. Fleischer, Substitutional solution hardening. *Acta Metall.* **11**(3), 203–209 (1963). [https://doi.org/10.1016/0001-6160\(63\)90213-X](https://doi.org/10.1016/0001-6160(63)90213-X)
  55. L. Kučerová, K. Burdová, Š. Jeníček, I. Chena, Effect of solution annealing and precipitation hardening at 250 °C–550 °C on microstructure and mechanical properties of additively manufactured 1.2709 maraging steel. *Mater. Sci. Eng. A* **814**, 141195 (2021). <https://doi.org/10.1016/j.msea.2021.141195>
  56. H.R. Lashgari, Y. Xue, C. Onggowarsito, C. Kong, S. Li, Microstructure, tribological properties and corrosion behaviour of additively manufactured 17–4PH stainless steel: effects of scanning pattern, build orientation, and single vs Double scan. *Mater Today Commun.* **25**, 101535 (2020). <https://doi.org/10.1016/j.mtcomm.2020.101535>
  57. F. Habiby, T.N. Siddiqui, H. Hussain, A. Ul Haq, A.Q. Khan, Lattice changes in the martensitic phase due to ageing in 18 wt% nickel maraging steel grade 350. *J. Mater. Sci.* **31**(2), 305–309 (1996). <https://doi.org/10.1007/BF01139144>
  58. S. Henschel, V. Kietov, F. Deirmina, M. Pellizzari, L. Krüger, Fracture toughness of a hot work tool steel-TiC composite produced by mechanical milling and spark plasma sintering. *Mater. Sci. Eng. A* **709**, 152–159 (2018). <https://doi.org/10.1016/j.msea.2017.10.053>
  59. R.O. Ritchie, On the interaction of cracks with bimaterial interfaces. *Mater. Sci.* **32**(1), 107–120 (1996). <https://doi.org/10.1007/BF02538931>
  60. V.X. de Lima Filho, T.N. Lima, S. Griza, B.R.C. Saraiva, H.F.G. de Abreu, The Increase of Fracture Toughness with Solution Annealing Temperature in 18Ni Maraging 300 Steel. *Mater. Res.* **24**(3), e20200472 (2021). <https://doi.org/10.1590/1980-5373-MR-2020-0472>

**Publisher's Note** Springer Nature remains neutral with regard to jurisdictional claims in published maps and institutional affiliations.